Martínez-Calvo, A., Moreno-Boza, D. & Sevilla, A. (2021). Non-linear dynamics and self-similarity in the rupture of ultra-thin viscoelastic liquid coatings. *Soft Matter*, 17(16), pp. 4363–4374.

DOI: 10.1039/d0sm02204g

Soft Matter

ARTICLE TYPE

Non-linear dynamics and self-similarity in the rupture of ultra-thin viscoelastic liquid coatings

A. Martínez-Calvo,[a] D. Moreno-Boza,[a] and A. Sevilla[a]

The influence of viscoelasticity on the dewetting of ultrathin polymer films is unraveled by means of theory and numerical simulations in the inertialess limit. Three viscoelastic models are employed to analyse the dynamics of the film, namely the Oldroyd-B, Giesekus, and FENE-P models. We revisit the linear stability analysis (LSA) first derived by [Tomar *et al.*, *Eur. Phys. J. E.*, 20, 185–200, 2006] for a Jeffreys film to conclude that all three models formally share the same dispersion relation. For times close to the rupture singularity, the self-similar regime recently discovered by [Moreno-Boza *et al.*, *Phys. Rev. Fluids*, 5, 014002, 2020], where the dimensionless minimum film thickness scales with the dimensionless time until rupture as $h_{\mathrm{min}} = 0.665\,\tau^{1/3}$, is asymptotically established independently of the rheological model. The spatial structure of the flow is characterised by a Newtonian core and a thin viscoelastic boundary layer at the free surface, where polymeric stresses become singular as $\tau \to 0$. The Deborah number and the solvent-to-total viscosity ratio affect the rupture time but not the length scale of the resulting dewetting pattern and asymptotic flow structure close to rupture, which is thus shown to be universal. Our three-dimensional simulations lead us to conclude that bulk viscoelasticity alone does not explain the experimental observations of dewetting of polymeric films near the glass transition.

1 Introduction

Thin liquid films can be found in a sheer number of technological applications, nature, and everyday phenomena. For instance, they play important roles in geological flows[1–3], medicine, or mammals physiology, where biofluids are present, as it is the case of surfactant-laden films covering the alveoli[4–10], or tear-film dynamics[11–15]. They are also involved in a myriad of engineering processes and applications, namely in coatings[16,17], patternings, or plasmonic devices[18–20], where films of micrometric or even nanometric thickness, usually referred to as *ultra-thin films*, are required. In particular, in many relevant configurations these thin films exhibit viscoelastic rheological behaviour, as is the case of tear films[11–15], or in polymeric solutions close to the glass transition[21].

In contrast with their Newtonian counterpart[22–27] and despite their practical relevance, the theory of unstable viscoelastic thin films remains largely unexplored. There are a few studies dealing with the development of the nascent vdW-triggered instability and its linear stability analysis (LSA). The seminal work[28] derives for the first time the dispersion relation of a Jeffreys-type film using the full equations of motion, including inertial effects. In particular, their analysis for zero inertial effects shows that in the limit of a polymeric melt, the growth rate experiences a singularity controlled by a critical Weissenberg number (the product of Capillary and Deborah numbers), upon which it blows up over a narrow band of wavelengths. This non-physical singularity reminds of a solid-like infinitely fast response to forcing, and is shown in[28] to be only overcome by including finite inertia of the liquid. In addition, electro-hydrodynamical effects are considered in the earlier work[29], which also encountered the aforementioned singularity.

By way of contrast, the lubrication approximation of the equations of motion incorporating viscoelastic models has been extensively used[30–34]. Alternatively, one aspect of the viscoelastic dewetting flow that has received considerable attention is the retraction dynamics of the liquid rims formed during the late stages of the film evolution[35–37]. However, the spatial structure of the thinning flow during the first stages of the spinodal dewetting process prior to the formation of the precursor film and liquid rim structures, most notably the associated rupture times and characteristic wavelengths, the possible existence of self-similar regimes appearing near the rupture singularity, and the performance of three-dimensional simulations, are all of them aspects that have not been studied as extensively as far as we know. Furthermore, the dewetting patterns observed in refs.[21,36,38] of polymeric films heated close to the glass transition are not yet fully understood. Here, we aim to address some of these questions by studying, for the first time, the linear stability derived from the complete Stokes

[a] *Grupo de Mecánica de Fluidos, Universidad Carlos III de Madrid, Av. Universidad 30, 28911 Leganés (Madrid), Spain; E-mail: amcalvo@ing.uc3m.es*

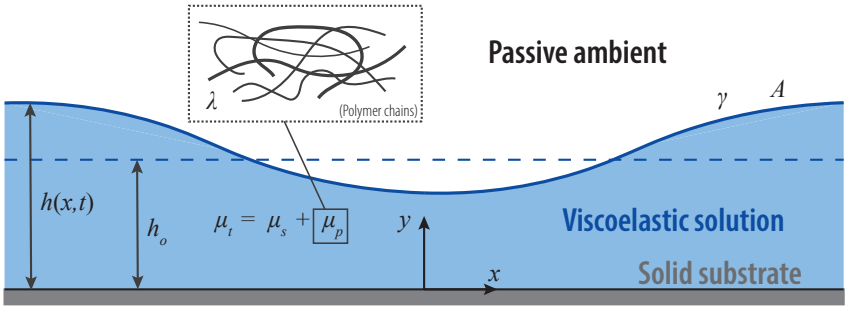

Fig. 1 Schematic of the flow configuration including the main parameters governing the problem and the coordinate system.

equations coupled with three viscoelastic constitutive equations, namely the Oldroyd-B, Giesekus, and FENE-P models. We then unveil the near-rupture dynamics, focusing on the existence of self-similarity and on the spatial structure of the dewetting flow using these three viscoelastic models. Finally, we perform three-dimensional direct numerical simulations to ask the following key question: Are the dewetting morphologies observed in glassy films a consequence of the viscoelastic rheology?

The paper is organised as follows. In §2 we present the mathematical models used to describe the dewetting flow of a viscoelastic ultra-thin films. In §3 we provide a linear stability analysis of the complete Stokes equations coupled with the different rheological models, and then we perform an comprehensive study comparing the latter results with previous ones obtained with the lubrication approximation. In §4 we carry out two-dimensional numerical simulations of the viscoelastic Stokes equations to unravel the asymptotic self-similar regimes during film thinning for different Deborah numbers and solvent-to-total viscosity ratios. We then focus on the viscoelastic self-similar problem in §?? to explain the observations made in §4. In §5 we provide three-dimensional direct numerical simulations of the complete viscoelastic Stokes equations to compare the dewetting patterns both with experiments and with their Newtonian counterpart. Concluding remarks are finally presented in §6.

2 Mathematical description

We consider the incompressible flow of a non-Newtonian thin liquid film initially resting on a solid substrate and immersed in a passive fluid ambient. It is well known that, in the non-wetting case, the van der Waals (vdW) intermolecular interactions between the film and the substrate induce the instability of the flat film solution when its initial height h_o is below approximately 100 nm. Indeed, the vdW forces exceed the stabilizing surface tension force for perturbations of sufficiently large wavelength, finally leading to film rupture[39,40]. Let γ denote the constant surface tension coefficient, μ_s the solvent viscosity, and μ_p the polymeric contribution to the viscosity, such that $\mu_t = \mu_s + \mu_p$ is the total effective viscosity and $\beta = \mu_s/\mu_t$ the solvent-to-total viscosity ratio. Note that $0 \leq \beta \leq 1$, where the limits $\beta \to 0$ and $\beta \to 1$ correspond to the cases of a polymer melt and a Newtonian film, respectively. By selecting

$$\ell_c = h_o, \quad v_c = \frac{A}{6\pi\mu_t h_o^2}, \quad t_c = \frac{6\pi\mu_t h_o^3}{A}, \quad p_c = \sigma_c = \phi_c = \frac{A}{6\pi h_o^3}, \tag{1}$$

as the relevant scales of length, velocity, time, pressure, stresses, and intermolecular potential, respectively, where A is the Hamaker constant[41], the dimensionless augmented[42] Stokes equations of motion read

$$\boldsymbol{\nabla}\cdot\boldsymbol{u} = 0, \quad \text{and} \quad \boldsymbol{0} = \boldsymbol{\nabla}\cdot(-\phi\boldsymbol{I} + \boldsymbol{T} + \boldsymbol{\sigma}), \quad \boldsymbol{x} \in \mathscr{V}, \tag{2}$$

where $\mathscr{V}$ is the fluid domain, $\boldsymbol{u}$ is the velocity field, $\phi = h^{-3}$ is the intermolecular potential derived for the particular case of the vdW force between two parallel surfaces, $\boldsymbol{T} = -p\boldsymbol{I} + 2\beta\boldsymbol{E}$ is the stress tensor of the fluid, $\boldsymbol{E} = 1/2\left(\boldsymbol{\nabla u} + \boldsymbol{\nabla u}^{\mathrm{T}}\right)$ is the rate-of-strain tensor, and $\boldsymbol{\sigma}$ is the symmetric polymeric stress tensor.

Historically, many constitutive equations have been used to determine the polymeric stress tensor (see refs.[43–46] for exhaustive reviews). One of the simplest and most commonly used models for dilute polymer solutions is the Oldroyd-B fluid, which can be derived from kinetic theory considering the polymer chains as non-interacting Hookean dumbbells. Here we only consider a single relaxation time of the chains, λ, in contrast with refs.[47–49], which introduced a discrete spectrum of relaxation times. However, as discussed by ref.[50], the assumption of a single relaxation time is a reasonable simplification, since the chains with the largest relaxation time eventually dominate the rate of stretching. The relaxation time λ immediately defines a Deborah number, $De = \lambda/t_c = A\lambda/(6\pi\mu_t h_o^3)$, as the ratio between λ and the relevant characteristic time scale t_c defined in eqn. (1). On selecting the scales (1), the dimensionless evolution equation for $\boldsymbol{\sigma}$ following the Oldroyd-B model reads

$$De\,\overset{\triangledown}{\boldsymbol{\sigma}} + \boldsymbol{\sigma} = 2(1-\beta)\boldsymbol{E}, \quad \boldsymbol{x} \in \mathscr{V}, \tag{3}$$

where $\overset{\triangledown}{\boldsymbol{\sigma}} = \partial_t\boldsymbol{\sigma} + \boldsymbol{u}\cdot\boldsymbol{\nabla\sigma} - (\boldsymbol{\nabla u})^{\mathrm{T}}\cdot\boldsymbol{\sigma} - \boldsymbol{\sigma}\cdot(\boldsymbol{\nabla u})$ is the upper-convected time derivative, defined for a tensor field. Equation (3) is a particular case of the general 8-constant model derived by Oldroyd[51]. Note that in the limit $\beta \to 0$ the solvent viscosity is small compared with the polymer viscosity, and eqn (3) reduces to the so-called upper-convected Maxwell model[51]. The linearisation of the upper-convected Maxwell and Oldroyd-B models yields the Maxwell's[52] and Jeffrey's[53] viscoelastic models, respectively. In contrast, the limit $\beta \to 1$ leads to the Stokes equations for a New-

tonian liquid as a particular case.

The Oldroyd-B model assumes that the dumbbells are infinitely stretchable, an approximation that may fail close to rupture as happens in the case of axisymmetric liquid threads[47,50,54]. Indeed, the finite extensibility of the polymer chains might affect the dewetting dynamics. More realistic models, that take into account such finite extensibility effects, are the FENE-P model[55], which stands for *finitely-extensible-nonlinear-elastic* and *P* for the Peterlin's closure idea[56], and the Giesekus model, first derived in ref.[57]. The polymeric constitutive equation in the FENE-P framework reads

$$De\,\overset{\triangledown}{\boldsymbol{\sigma}}+\left[\frac{1}{1-3/L^2}+\frac{De}{(1-\beta)L^2}\mathrm{tr}(\boldsymbol{\sigma})\right]\boldsymbol{\sigma}=\frac{2(1-\beta)}{1-3/L^2}\boldsymbol{E},\ \boldsymbol{x}\in\mathscr{V},\quad(4)$$

where the dimensionless parameter L^2, usually known as the extensibility parameter, denotes the ratio between the maximum length and the equilibrium length of the dumbbells, which is in turn a function of the spring constant, the Boltzmann constant, and the temperature. In the infinitely extensible limit, $L\to\infty$, the Oldroyd-B model (3) is recovered. Finally, the third model considered in the present work is the Giesekus model, whose associated constitutive equation reads

$$De\,\overset{\triangledown}{\boldsymbol{\sigma}}+\boldsymbol{\sigma}+\frac{De\,\alpha}{1-\beta}(\boldsymbol{\sigma}\cdot\boldsymbol{\sigma})=2(1-\beta)\boldsymbol{E},\quad \boldsymbol{x}\in\mathscr{V},\qquad(5)$$

where α is a dimensionless parameter that accounts for the anisotropy of the drag coefficient of the polymer chains within the fluid. In the limit $\alpha\to 0$, it reduces to the Oldroyd-B model (3).

At the free surface, $\boldsymbol{x}\in\partial\mathscr{V}$, we impose the kinematic condition, which precludes interfacial mass transfer, and the surface stress balance,

$$\boldsymbol{n}\cdot(\partial_t\boldsymbol{x}_s-\boldsymbol{u})=0,\qquad(6a)$$

$$(\boldsymbol{T}+\boldsymbol{\sigma})\cdot\boldsymbol{n}+Ca^{-1}\boldsymbol{n}(\boldsymbol{\nabla}\cdot\boldsymbol{n})=\boldsymbol{0},\qquad(6b)$$

respectively, where $Ca=A/(6\pi\gamma h_o^2)$ is the Capillary number, which can be expressed in terms of the *molecular length*[58], $a=[A/(6\pi\gamma)]^{1/2}$, as $Ca=(h_o/a)^{-2}$. Here $\boldsymbol{x}_s$ is the parametrisation of the free surface, and $\boldsymbol{n}$ its unit normal vector. At the solid substrate, the no-slip and no-penetration boundary conditions, $\boldsymbol{u}=\boldsymbol{0}$, are fulfilled.

3 Linear stability analysis

To analyse the effect of viscoelasticity on the initial growth of perturbations, we perform a linear stability analysis of the wdW-unstable viscoelastic film considering, for the first time, the complete equations of the different rheological models. The results will then be compared with those obtained from the lubrication theory developed in refs.[30,32].

3.1 Stokes equations

The dispersion relation is derived by introducing the normal-mode decomposition

$$(\boldsymbol{u},p,h,\boldsymbol{\sigma})=(\boldsymbol{0},0,1,\boldsymbol{0})+\varepsilon(\hat{\boldsymbol{u}},\hat{p},\hat{h},\hat{\boldsymbol{\sigma}})e^{\omega t+ikx}+O(\varepsilon^2),\qquad(7)$$

into eqns (2), (6a), (6b), and either (3), or (4), or (5), and retaining terms up to $O(\varepsilon)$, where $\varepsilon\ll 1$ is the relative amplitude of the perturbation, ω is the growth rate, which should be understood as a real quantity[28], and k is the wavenumber. The dispersion relation is therefore given by

$$(1+De\omega)(Ca^{-1}k^2-3)(\sinh(2k)-2k)+$$
$$2\omega k(1+\beta De\,\omega)[\cosh(2k)+2k^2+1]=0.\qquad(8)$$

Its explicit solution for the temporal growth rate $\omega(k)$ is provided in appendix A. Ref.[28] studied the linear stability of a viscoelastic vdW-unstable film described by the linear Jeffrey's model, which should yield the same dispersion relation as (8), but perhaps due to errors or typos in their derivation these authors obtained a dispersion relation with missing terms.

It is important to emphasise that the Giesekus model yields exactly the same dispersion relation, since the term proportional to α is non-linear and the base-flow velocity is zero. In the case of the FENE-P constitutive equation, the functional form of the dispersion relation is also the same, but the Deborah number has to be redefined as $De\to De(1-3/L^2)$. Notice also that in the limits $De\to 0$ or $\beta\to 1$, eqn (8) yields the growth rate corresponding to a Newtonian film, namely $\omega=(3-Ca^{-1}k^2)[\sinh(2k)-2k]/[2k(1+2k^2+\cosh(2k))]$, deduced for instance in refs.[27,59].

Figure 2 shows the amplification curves $\omega(k)$ obtained from eqn (27), for $\beta=(0,0.1,0.5,0.9)$ in panels 2(*a–d*), respectively, for different values of De indicated in the legends. The filled circles are the growth rates extracted from the two-dimensional numerical simulations by imposing the corresponding wavenumber and streamwise periodicity conditions (more details are provided in § 4), displaying excellent agreement. The most remarkable feature of fig. 2 is the fact that the most amplified wavenumber, k_m, is independent of the rheological parameters and depends only on Ca, which can be readily explained by noticing that the viscoelastic parameters β and De only appear in the coefficients of ω and ω^2 in (8), as already noted in[28,34] in their analyses. Indeed, one can find an implicit equation for k_m upon maximizing the solution given in Appendix A, eqn (27), with respect to k. This in fact yields a product of two separate functions of k_m, one of which only vanishes for $k_m=0$. The non-trivial factor yields the transcendental equation

$$0=6Cak_m\left(4k_m^2+1\right)+2k_m^3+$$
$$2k_m\left[Ca\left(6k_m^2+3\right)+k_m^2(1-2k_m^2)\right]\cosh(2k_m)-$$
$$\left(3Ca+k_m^2\right)\left[2k_m^2+\cosh(2k_m)+1\right]\sinh(2k_m),\qquad(9)$$

which indeed shows that k_m depends exclusively on Ca, as suggested by the results of Figs. 2(*a–d*). Consequently, the characteristic length of the dewetting patterns should not be affected by the viscoelasticity of the film. Although eqn (9) has no closed-form solution for k_m, a small-Ca expansion provides

$$k_m=\sqrt{\frac{3Ca}{2}}\left[1-\frac{27}{40}Ca+\frac{36873}{22400}Ca^2+O(Ca^3)\right],\qquad(10)$$

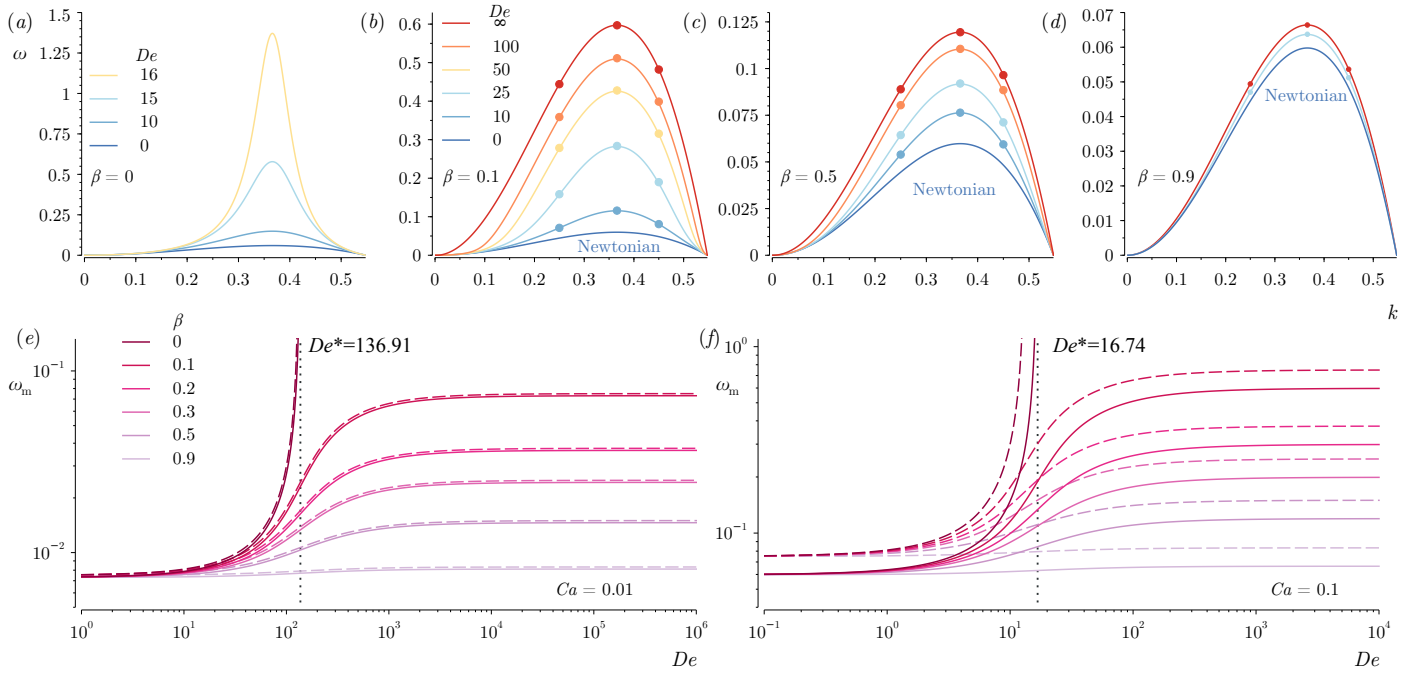

Fig. 2 Amplification curves $\omega(k)$ for $Ca = 0.1$ ($h_o/a = 3.16$) and (a) $\beta = 0$, (b) 0.1 and (c) 0.5 and (d) 0.9, and different values of De indicated in the legends. The symbols indicate the results extracted from the two-dimensional numerical simulations of Stokes equations (22a) coupled with the Oldroyd-B model (3). Panels (e) and (f) show the maximum growth rate, ω_m, obtained numerically from the exact dispersion relation (8) (solid lines), and the analytical solution (19) obtained from the lubrication approximation (dashed lines), taking $Ca = 0.01$ ($h_o/a = 10$) and $Ca = 0.1$ ($h_o/a = 3.16$) in (e) and (f), respectively.

which, to leading order, effectively recovers the well-known result from lubrication theory $k_m/k_c = 1/\sqrt{2}$, where $k_c = \sqrt{3Ca}$ is the cut-off wavenumber[39]. Also from the linear analysis we can obtain the fastest growth rate of perturbations corresponding with the most amplified wavenumber, ω_m, and thus an estimation of the rupture time, $t_R \sim \ln(\varepsilon^{-1})/\omega_m$ (see for instance ref.[22]). Fig. 3 shows a comparison between the rupture times obtained from the numerical integration of (2) and those stemming from the linear prediction, namely, $t_R \sim \ln(\varepsilon^{-1})/\omega_m$. In an effort to give an analytical prediction for t_R, we first derive the small-k expansion from (27)

$$\omega = k^2 + \left[De(1-\beta) - \frac{1}{3Ca} - \frac{9}{5}\right]k^4 + \left[\frac{3[7(\beta-1)De(10\beta De - 5De + 18) + 115]}{105} + \frac{70(\beta-1)De + 63}{105Ca}\right]k^6 + O(k^8) \quad (11)$$

which enables us to obtain an estimate of the rupture time, t_R, by substituting the expression for k_m in eqn (10) into the above equation

$$\frac{t_R}{\ln(\varepsilon^{-1})} = \frac{4}{3Ca} + \frac{18}{5} - \frac{3Ca}{700}\{2899 + 140(\beta-1)De\,[27 + 5De(5\beta-3)]\} + O(Ca^2). \quad (12)$$

From the expression above we can infer that the rupture time t_R and, in consequence, the maximum growth rate ω_m, are slightly affected by the viscoelastic effects if the capillary number Ca is small or, in other words, if the initial film height is much larger than the molecular length scale, $h_o/a \gg 1$, as clearly observed in Figs. 2(e) and (f). Indeed, eqn (12) reveals that De and β appear in terms which are $O(Ca)$ and higher in the Ca-expansion.

It proves useful to provide the expression of the rupture time scaled with the characteristic time $t_c = \mu_t a/\gamma$, which makes use of the molecular length scale a instead of the initial film thickness h_o. In particular, we note here that the use of a as substitution for h_o in the characteristic scales is useful to analyse the non-linear dynamics of the flow near rupture, studied in §4. Expressing $\bar{t}_R$ rescaled with t_c as a function of h_o/a instead of Ca yields [27,58,60],

$$\frac{\bar{t}_R}{\ln(\varepsilon^{-1})} = \frac{4}{3}\left(\frac{h_o}{a}\right)^5 + \frac{18}{5}\left(\frac{h_o}{a}\right)^3 - \frac{3}{700}\frac{h_o}{a}\{2899 + 140(\beta-1)De\,[27 + 5De(5\beta-3)]\} + O\left[\left(\frac{h_o}{a}\right)^{-1}\right]. \quad (13)$$

It is also interesting to note that the dispersion relation (8) is exactly the same as the one obtained from linear viscoelastic models, namely the Jeffreys's[28] and Maxwell's models, when taking the limit of a polymer melt, $\beta \to 0$, and arbitrary De, which reads

$$\omega = \frac{(3 - k^2Ca^{-1})[\sinh(2k) - 2k]}{De(3 - k^2Ca^{-1})[2k - \sinh(2k)] + 2k[\cosh(2k) + 2k^2 + 1]}. \quad (14)$$

Note that the maximum growth rate ω_m becomes singular in this limit when $De \simeq De^* \equiv 4/(3Ca) + 18/5 - 1797\,Ca/700$ as provided

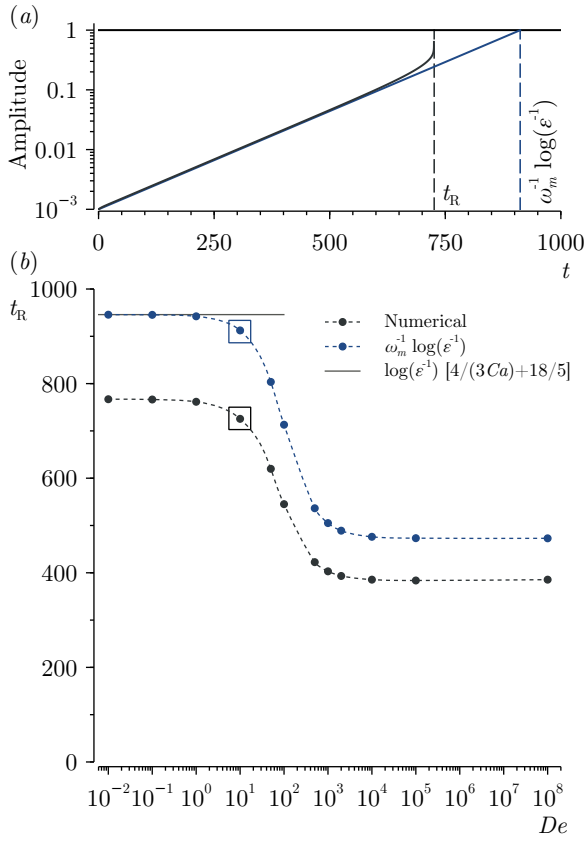

Fig. 3 Determination of the rupture time. (*a*) Temporal evolution of the amplitude of the initial perturbation compared with the prediction provided by the LSA. (*b*) Rupture time t_R as a function of the Deborah number De extracted from the time-dependent numerical simulations and the estimation from the linear stability theory. Although LSA overpredicts t_R, the parametric dependence on the rest of parameters (not shown here) is qualitatively well captured. Computations are for an Oldroyd-B film with $\varepsilon = 10^{-3}$, $Ca = 0.01$ and $\beta = 0.5$. The squares in the lower panel corresponds to the case shown in the upper panel.

by substituting $k = k_m \simeq \sqrt{3Ca/2}\,(1 - 27\,Ca/40)$ in eqn (14). The appearance of such *critical* value of De and the subsequent singularity in the temporal growth rate has been previously discussed in[28,29,34], where a solid-like behaviour is accompanied by an almost instantaneous response to an applied forcing. Liquid inertia is seen to be a regularization mechanism, as demonstrated in[28]. Fig. 2(*a*) shows the temporally unstable branch for increasing values of De, where a peak at $k = k_m$ is seen to develop as $De \to De^*$. In figs. 2 (*e*) and (*f*) this singularity is displayed for the maximum growth rate ω_m, which diverges as $(De - De^*)^{-1}$ for $\beta = 0$. In this limiting case, the dynamics is completely dictated by the polymer melt, which behaves as a viscoelastic solid. Nevertheless, the limit of eqn (14) when $De \to \infty$ yields $\omega \to 0$, since the polymer chains never relax due to the fact that $\lambda \gg t_c$.

In the limit $De \to \infty$ and arbitrary β, the dispersion relation (8) reduces to

$$\omega = \frac{(k^2 Ca^{-1} - 3)[2k - \sinh(2k)]}{2\beta k[\cosh(2k) + 2k^2 + 1]}, \tag{15}$$

and $\omega \sim \beta^{-1}$. Here, since $\lambda \gg t_c$, the polymer chains neither relax nor do they contribute to the viscosity of the suspension (see eqn 3). Hence, the appropriate time scale only involves the viscosity of the solvent μ_s, and the growth rate should be rescaled as $\omega \to \beta\omega$, which yields a parameter-free amplification curve with the same functional form as that of a Newtonian film.

3.2 The lubrication approximation

Under the lubrication approximation of the Jeffrey's model, the equivalent expressions of eqns (8) and (15) were first obtained by Safran and Klein[30], and refined later on by Blossey *et al.*[32] considering also wall slippage. Neglecting slippage, the dispersion relation obtained from the lubrication model reads

$$\omega\,(1 + De\beta\omega) - (1 + De\omega)\,(3 - Ca^{-1}k^2)\,k^2/3 = 0. \tag{16}$$

This lubrication dispersion relation can be also derived from eqn (8) by expanding in powers of k, resulting in an identical expression except for the order $O(k^4)$ term, $-9/5$. From eqn (16) we can take the limit $De \to \infty$,

$$\omega = \frac{k^2(3 - Ca^{-1}k^2)}{3\beta}, \tag{17}$$

to be compared with its Stokes counterpart (15). Note that, in ref.[32], our parameter β is equivalent to the ratio between their λ_2 and λ_1 time scales, which are the relaxation times associated to the viscous rate-of-strain of the solvent and to the polymeric stress, respectively. In addition, the limit $\beta \to 0$ of a polymer melt, under the lubrication approximation, reads

$$\omega = \frac{k^2(3 - Ca^{-1}k^2)}{Dek^2(Ca^{-1}k^2 - 3) + 3}, \tag{18}$$

to be compared with the corresponding Stokes result (14).

From the lubrication dispersion relations (16)–(18) we can obtain the most amplified wavenumber, which is independent of De and β as anticipated from the full Stokes equations in eqns (9),

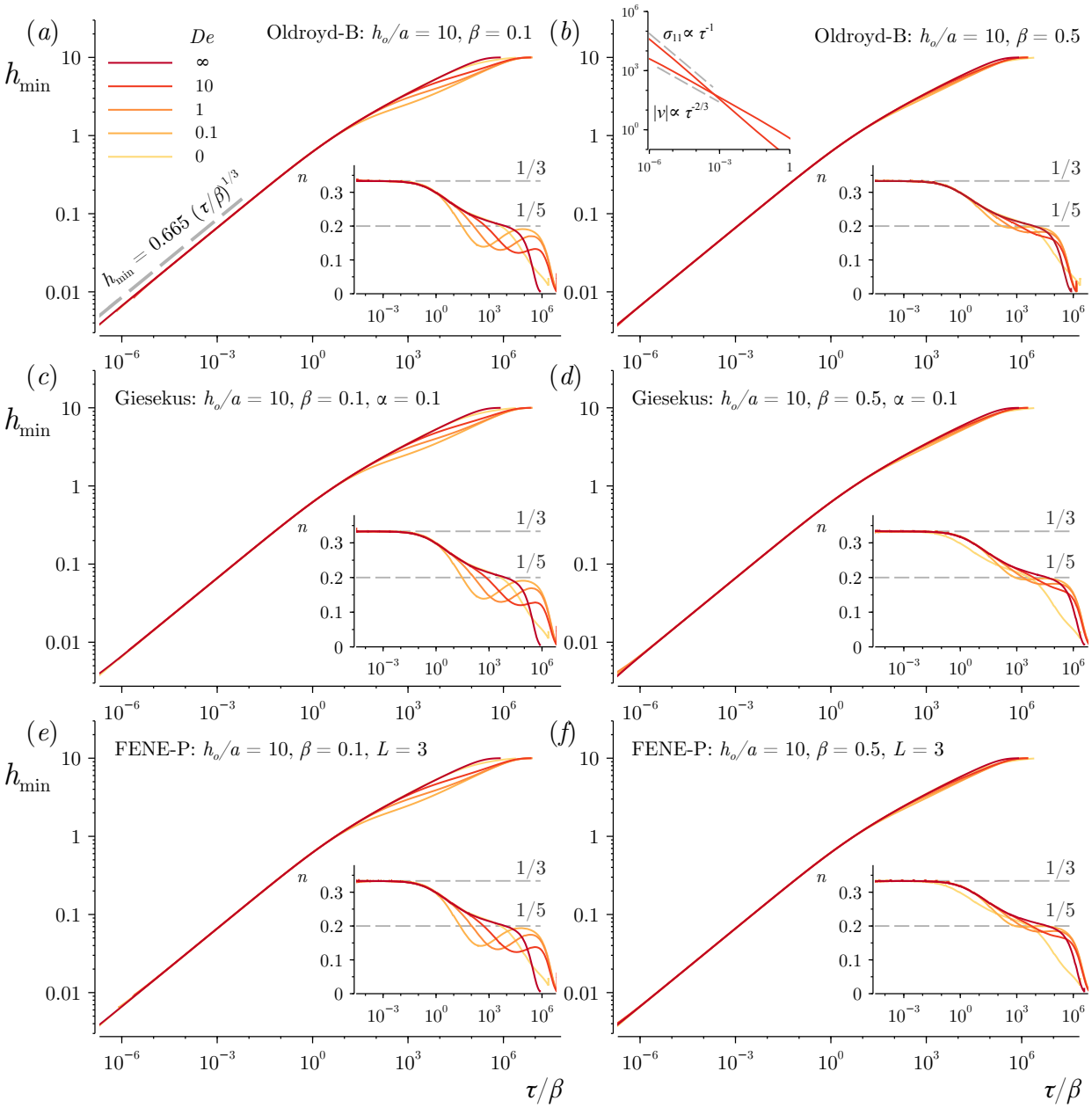

Fig. 4 Minimum film thickness as a function of the rescaled time to rupture, τ/β for different values of the Deborah number, De, indicated in the legend, and $\beta = 0.1$ in (a,c,e), and $\beta = 0.5$ in (b,d,f), and the three different viscoelastic models, namely Oldroyd-B in (a,b), Giesekus in (c,d), and FENE-P in (e,f). The lower insets show the corresponding instantaneous exponents $n = \mathrm{d}\log_{10} h_{\min}/\mathrm{d}\log_{10}(\tau/\beta)$ as a function of τ/β. The upper inset in (b) illustrates the consistent τ^{-1}-, $\tau^{-2/3}$-, and $\tau^{-1/2}$-behaviours of the polymeric stress σ_{11}, vertical velocity $|v|$, and transversal increments $\Delta_T v$, respectively, evaluated at $x = 0$, $y = h_{\min}(t)$ for $De = 10$.

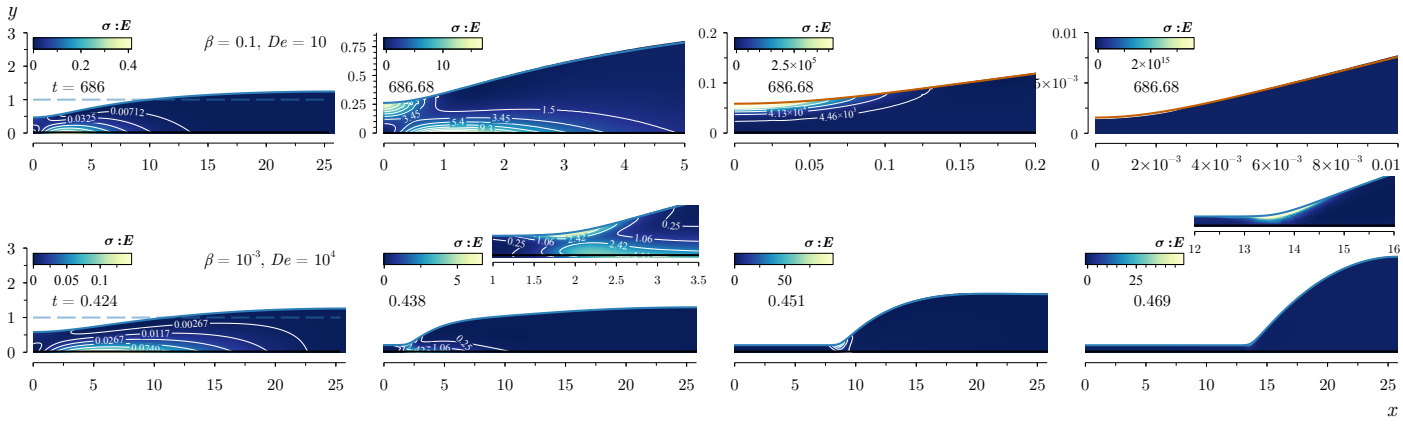

Fig. 5 Snapshots of the evolution of a viscoelastic thin liquid film with $Ca = 0.01$ (or $h_o/a = 10$), where the color plot shows the scalar quantity $\boldsymbol{\sigma} : \boldsymbol{E}$, with $\beta = 0.1$ and $De = 10$ in (a–d), and $\beta = 10^{-3}$ and $De = 10^4$ in (e–h). Here, lengths, time t and $\boldsymbol{\sigma} : \boldsymbol{E}$ have been scaled with (1).

$k_m = \sqrt{3Ca/2}$. The corresponding maximum growth rates read

$$\omega_m = \frac{3CaDe - 4 + \sqrt{(4-3CaDe)^2 + 48CaDe\beta}}{8De\beta}, \tag{19a}$$

$$\omega_m = \frac{3Ca}{4\beta}, \tag{19b}$$

$$\omega_m = \frac{3}{4Ca^{-1} - 3De}, \tag{19c}$$

as obtained from eqs (16)–(18), respectively. Interestingly, from the polymer melt limit in eqn (19c) it is possible to estimate the value of De for which the maximum growth rate diverges, as shown in Figs. 2(a), (e), and (f), yielding $De \simeq 4/(3Ca)$.

4 Nonlinear and near-rupture dynamics

4.1 Numerical simulations

To elucidate the nonlinear and near-rupture dynamics of the viscoelastic thin film, we have performed numerical simulations of the complete Stokes equations (2), coupled with either the Oldroyd-B (3), Giesekus (5), or FENE-P (4) models for the polymeric stress tensor. Taking into account the fact that the local flow close to the rupture singularity loses memory of the initial conditions, it proves convenient to change the characteristic length scale to non-dimensionalise the mathematical model, substituting h_o by a,

$$\ell_c = a = \sqrt{\frac{A}{6\pi\gamma}}, \quad t_c = \frac{\mu_t a}{\gamma}, \quad v_c = \frac{\gamma}{\mu_t}, \quad p_c = \sigma_c = \phi_c = \frac{A}{6\pi a^3} \tag{20}$$

We consider first a planar two-dimensional film starting from rest and whose free surface is slightly perturbed by a harmonic disturbance at $t = 0$, namely

$$\boldsymbol{u}(\boldsymbol{x},0) = \boldsymbol{0}, \quad h(x,0) = h_o/a(1 - \varepsilon\cos kx) \quad \text{with} \quad k < k_c, \tag{21}$$

for $0 \le x \le \pi/k$, thus triggering the vdW-induced instability. The numerical method was adapted from the one employed in refs.[27,60], where the reader can find a detailed technical explanation. The scales used to study the near-rupture dynamics are the molecular scales (20), unless otherwise specified.

Fig. 4 shows the minimum thickness of the film, $h_{\min} = h(x,0)$, and the instantaneous exponent $n = \mathrm{d}\log_{10}h_{\min}/\mathrm{d}\log_{10}(\tau/\beta)$ in the insets, as functions of the rescaled time to rupture, $\tau/\beta = (t_R - t)/\beta$. In particular, Figs. 4(a,b) show the results obtained from the Oldroyd-B model, Figs. 4(c,d) those from the Giesekus model, and Figs. 4(e,f) those from the FENE-P model. These figures evidence that, independently of the viscoelastic constitutive equation and for any value of β, De, L^2 and α, the ultimate self-similar regime that is established as $\tau \to 0$ is that of a Newtonian liquid film, recently discovered in ref.[27], and where $h_{\min} = 0.665\bar{\tau}^{1/3}$, where $\bar{\tau} = \tau/\beta$ is the time to rupture non-dimensionalised with the viscosity of the Newtonian liquid. Hence, the fact that τ/β is the appropriate time that makes all the interface evolutions collapse close to rupture means that only the solvent plays a role close to the singularity. More importantly, to elucidate how the polymeric stresses affect the transient regime and the spatial structure of the flow as the singularity is approached, Fig. 5 shows the evolutions of two different viscoelastic films with $Ca = 0.01$ (or $h_o/a = 10$), where the coloured contours display the scalar quantity $\boldsymbol{\sigma} : \boldsymbol{E}$, which indicates the regions where the polymer chains are more or less elongated[61]. The values of the parameters are $\beta = 0.1, De = 10$ in Figs. 4(a–d), and $\beta = 10^{-3}, De = 10^4$ in Figs. 4(e–h). Note also that a precursor film of dimensionless height $h_{\text{prec}} = 0.1$ has been incorporated in these simulations (see eqn (25) below). Close enough to the rupture singularity, typically for $h_{\min} \lesssim 0.1$, the flow is organised in a two-region structure, composed of a Newtonian core and a viscoelastic boundary layer at the interface, where the polymeric stresses are confined and become singular as rupture is approached. The confinement of the polymeric stresses within a very thin layer explains their negligible influence in the global dynamics of the film when $\tau \ll 1$, and also the fact that the asymptotic flow structure is unaffected by the viscoelastic rheology of the film, which coincides with the universal solution for Newtonian liquids described in detail in ref.[27].

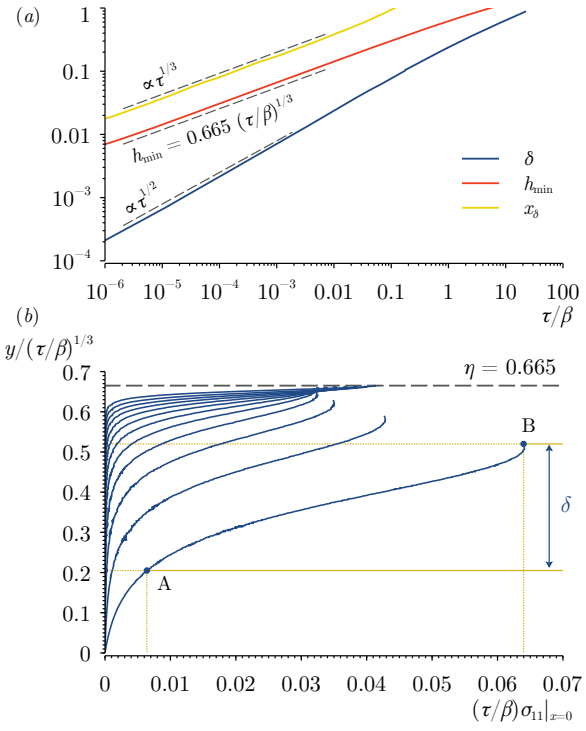

Fig. 6 (*a*) Evolution of the viscoelastic boundary layer thickness $\delta(\tau) \propto \tau^{1/2}$, shown to follow a faster thinning than that of the minimum film thickness $h_{\min}(\tau) \propto \tau^{1/3}$, and lateral length scale $x_\delta \propto \tau^{1/3}$. (*b*) Axial evolution of the re-scaled polymeric stress $\sigma_{11}|_{x=0}$ at times $\tau = (10.96, 1.633, 0.343, 0.087, 0.024, 0.007, 0.0021, 0.0006, 0.00019, 0.000062, 0.000019)$. The 10%-criterion to retrieve δ is also illustrated by means of the points A and B for which $0.1\sigma_{\max} \leq \sigma_{11} \leq \sigma_{\max}$, with $\sigma_{\max}(\tau)$ the instantaneous maximum of the polymeric stress. A similar strategy is used to compute x_δ, but evaluating σ_{11} in the free surface instead. Computations are for an Oldroyd-B film with $h_o/a = 10$, $\beta = 0.5$, $De = 10$.

4.2 Near-rupture flow and viscoelastic boundary layer

The results of section 4.1 will now be explained by means of a careful analysis of the simulation results for $\tau \ll 1$. The projection of the momentum equation (2) in the x-direction can be estimated at the scale of the film, $y \sim h_{\min}$, to yield the balance $-\partial_x \phi \sim \partial^2_{xx} u \Rightarrow h_{\min}^{-4} \sim u_c/x_c^2 \sim (h_{\min}\tau)^{-1}$, leading to the asymptotic rupture law $h_{\min} \sim \tau^{1/3}$ deduced in[27], and confirmed in the viscoelastic flow under study by the results of Fig. 4. The x-momentum equation can also be used to estimate the characteristic polymeric stresses, $\sigma_c(\tau)$. Indeed, $-\partial_x \phi \sim \partial_x \sigma_{11} \Rightarrow \sigma_c \sim \phi_c$, where $\phi_c \sim h_{\min}^{-3}$ is the characteristic van der Waals potential, leading to $\sigma_c \sim \tau^{-1}$, in agreement with the inset of Fig. 4(b). The thickness and length of the viscoelastic boundary layer, respectively given by $\delta(\tau)$ and $x_\delta(\tau)$ (see Figs. 8 and 9), were obtained from the evaluation of the spatial distribution of the polymeric stresses for decreasing vales of τ. Figure 6(b) shows the distribution of the rescaled polymeric stress $(\tau/\beta)\sigma_1 1$ as a function of the rescaled transverse coordinate, $(\beta/\tau)^{1/3}y$, and evaluated at the symmetry plane, $x = 0$.

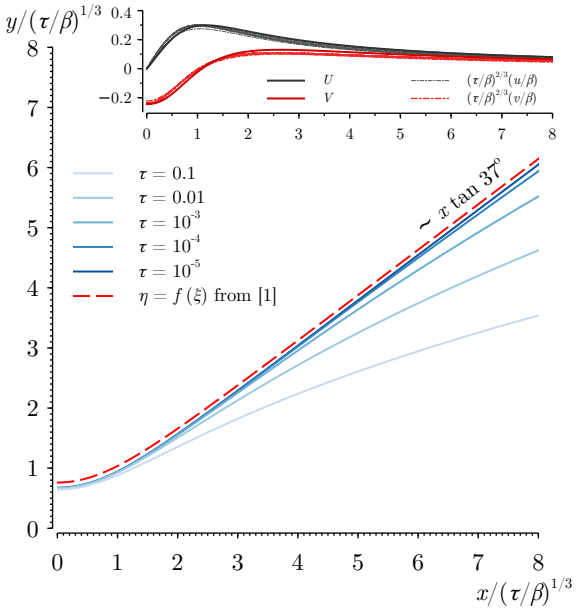

Fig. 7 Self-similar collapse of the film shapes (main panel) and velocities (upper inset) for a Giesekus film with $h_o/a = 10, \beta = 0.5, De = 10, \alpha = 0.1$ (solid lines). As $\tau \to 0$, collapse is achieved towards the self-similar solution $\eta = f(\xi)$, with $f(0) \simeq 0.665$, and U and V, obtained by the integration of (22a)–(24c), previously reported in[27] (dashed line). A small vertical offset has been added to the function $f(\xi)$ to make it distinguishable from the numerical profiles.

4.3 The leading-order self-similar solution

In view of the results of Fig. 4, one may anticipate the appearance of a self-similar regime in which $h_{\min}$ follows the asymptotic thinning law first reported in our previous work[27], namely $h_{\min} \propto \tau^{1/3}$, whereas the maximum velocity should scale as $u \propto \tau^{-2/3}$. Moreover, this law is expected to be achieved for arbitrary values of De and $\beta > 0$, according to the non-linear simulations. The self-similar exponents numerically obtained resemble those obtained in ref.[27], in which the Stokes equations exhibit a similarity solution of the first kind with a wedge-shaped free surface and an associated opening angle of 37° off the solid substrate. In what follows, we shall demonstrate that viscoelastic film thinning is dictated by the same asymptotic law as that of a Newtonian liquid. The leading-order description of the fluid flow is the same as that given in ref.[27] whereas the viscoelastic stress tensor is seen to obey a homogeneous problem whose solution, at leading order in powers of τ, is the trivial one $\boldsymbol{\sigma} \to \boldsymbol{0}$ as $\tau \to 0$. Indeed, by letting $x = (\tau/\beta)^{1/3}\xi$, $y = (\tau/\beta)^{1/3}\eta$, $u = (\tau/\beta)^{-2/3}\beta U$, $v = (\tau/\beta)^{-2/3}\beta V$, $p = (\tau/\beta)^{-1}P$, $h = (\tau/\beta)^{1/3}f(\xi)$ and $\sigma_{ij} = (\tau/\beta)^{-1}\Sigma_{ij}$, with i (or j) $= (1,2)$, one finds the consistent leading-order elliptic system of partial differential equations

$$U_\xi + V_\eta = 0, \tag{22a}$$

$$U_{\xi\xi} + U_{\eta\eta} + \Sigma_{11,\xi} + \Sigma_{12,\eta} = P_\xi - \frac{3f_\xi}{f^4}, \tag{22b}$$

$$V_{\xi\xi} + V_{\eta\eta} + \Sigma_{12,\xi} + \Sigma_{22,\eta} = P_\eta, \tag{22c}$$

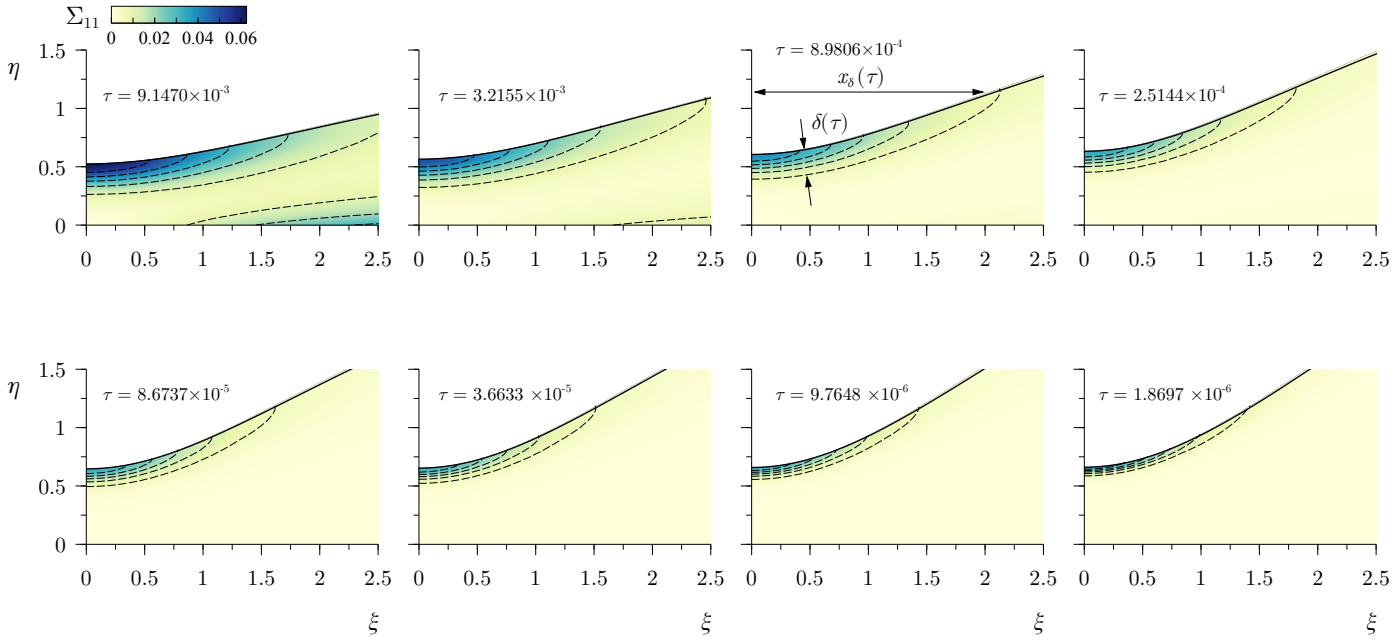

Fig. 8 Re-scaled temporal evolutions showing the self-similar collapse of the film shapes of an Oldroyd-B film with $h_o/a = 10, \beta = 0.5, De = 10$. The colour plots and contours show the self-similar viscoelastic stress $\Sigma_{11} = \tau\sigma_{11}$, which is confined to a boundary layer at the free surface as $\tau \to 0$, as the remaining components of the viscoelastic stress tensor.

stemming from eqn (2), to be integrated in $-\infty < \xi < \infty$ and $0 < \eta < f(\xi)$, where $f(\xi)$ is to be obtained as part of the solution. Eqns (22a)–(22c), need to be integrated with the boundary conditions (6), which in self-similar variables read

$$(1+f_\xi^2)P - f_\xi^2\left(\Sigma_{11} - 2U_\xi\right) - 2\left(\Sigma_{22} + 2V_\eta\right) + 2f_\xi\left(\Sigma_{12} + U_\eta + V_\xi\right) = 0, \tag{23a}$$

$$f_\xi\left[\Sigma_{22} - \Sigma_{11} + 2\left(V_\eta - U_\xi\right)\right] + (1-f_\xi^2)\left(\Sigma_{12} + U_\eta + V_\xi\right) = 0, \tag{23b}$$

$$f + 3V - (\xi + 3U)f_\xi = 0, \tag{23c}$$

along the free surface $\eta = f(\xi)$, $U = V = 0$ at the substrate wall $\eta = 0$, and $U = 0$ at the symmetry axis $\xi = 0$. The remaining boundary conditions at the numerical infinity $\xi \gg 1$ are handled as in ref.[27]. Note that capillarity forces are subdominant, and the leading-order balance is established between viscous and vdW forces. In addition, it is important to emphasise that eqns (22a)–(23c) are independent of the viscoelastic model. For instance, the Oldroyd-B model yields the system of equations

$$(\xi+3U)\Sigma_{11,\xi} + (\eta+3V)\Sigma_{11,\eta} + (3-6U_\xi)\Sigma_{11} - 6U_\eta\Sigma_{12} = 0, \tag{24a}$$

$$(\xi+3U)\Sigma_{12,\xi} + (\eta+3V)\Sigma_{12,\eta} - 3\left(V_\xi\Sigma_{11} - \Sigma_{12} + U_\eta\Sigma_{22}\right) = 0, \tag{24b}$$

$$(\xi+3U)\Sigma_{22,\xi} + (\eta+3V)\Sigma_{22,\eta} + (3-6V_\eta)\Sigma_{22} - 6V_\xi\Sigma_{12} = 0, \tag{24c}$$

at $O(\tau^{-2})$, which completes the self-similar description. The system formed by eqns (24a)–(24c) constitutes a homogeneous linear system for the components of the leading-order polymer stress tensor Σ_{ij}, independent of De and β. Note that the trivial solution $\Sigma_{ij} = 0$ yields the solution given in ref.[27] for the flow field, providing a free surface whose far-field shape is linear, i.e., $f = (\xi - \xi_o)\tan\theta_o$, for some ξ_o, compatible with eqn (23c) for $\xi \gg 1$ and vanishing velocities. The numerical solution of eqns (22a)–(24c) (see ref.[27] for details on the numerical method) confirms that this angle is indeed $\theta_o \sim 37°$, with accompanying vanishing polymeric stresses. The self-similar collapse is illustrated in Fig. 7 for a Giesekus film with no precursor. The study of the rheological boundary layer sitting on the free surface $\eta = f(\xi)$ appearing at the following order would constitute a formidable mathematical task, intrinsic to each viscoelastic model, and not to be pursued in this paper.

5 Three-dimensional numerical simulations

The experimental patterns shown in refs.[21,36,38] are thus far unexplained. To elucidate if these patterns arising in polymeric films

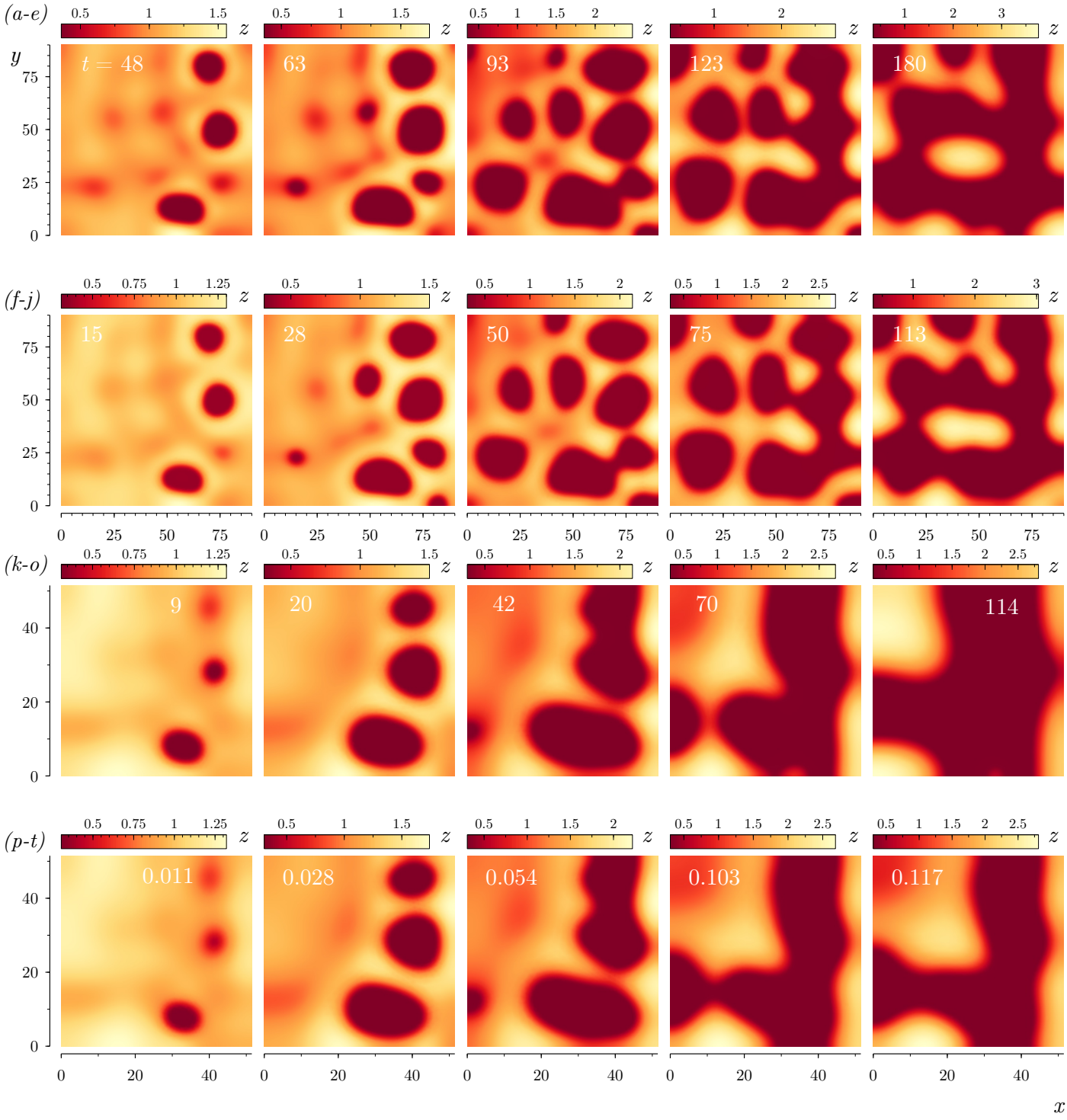

Fig. 9 Evolutions of a three-dimensional thin liquid film with $h_o/a = 5$, $\varepsilon = 0.05$, and $h_{\text{prec}} = 0.35$ in (a–j), and $\varepsilon = 0.1$, $h_{\text{prec}} = 0.3$ in (k–t). Colours represent the local film thickness $z = h(x,y)$. The Newtonian liquid film is shown in (a-e), and the non-Newtonian films are shown in the remaining panels with the corresponding viscoelastic dimensionless numbers being (f-j) $\beta = 0.1$ and $De = 10$, (k-o) $\beta = 0.1$ and $De = 1$, and (p–t) $\beta = 10^{-3}$ and $De = 100$. The labels indicating time are scaled with (1).

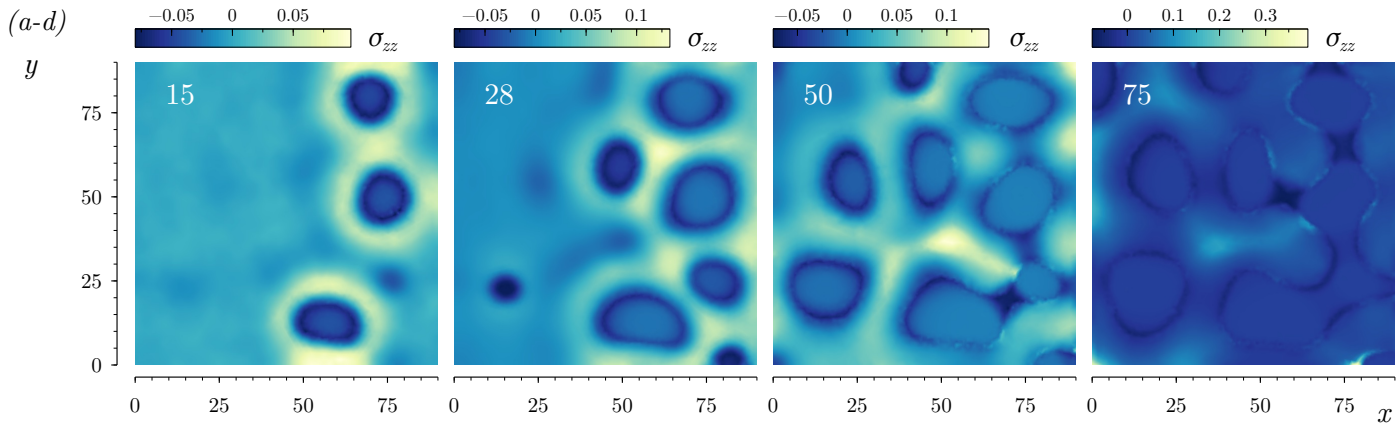

Fig. 10 Evolution of the σ_{zz} viscoelastic stress at the liquid-air interface of a three-dimensional thin liquid film with the same parameters as in fig. 9 (*a*–*e*), namely $h_o/a = 5$, $\varepsilon = 0.05$, and $h_{\text{prec}} = 0.35$, $\beta = 0.1$ and $De = 10$. The labels indicating time are scaled with (1).

heated close to the glass transition are due to a viscoelastic behaviour, we perform three-dimensional direct numerical simulations of the Oldroyd-B model with the addition of a short-range potential such that the intermolecular potential may be replaced by

$$\phi = h^{-3} - h_{\text{prec}}^6 h^{-9} \tag{25}$$

(see for instance ref.[26]) in eqns (2), where h_{prec} is the dimensionless thickness of the precursor film. As for the three-dimensional initial condition, we impose a randomly corrugated surface and zero velocity,

$$h(\boldsymbol{x}_{||},0) = 1 + \sum_{|i|\leq M}\sum_{|j|\leq N} A_{ij}\cos\left(\boldsymbol{k}_{ij}\cdot\boldsymbol{x}_{||} + \mathscr{U}\right), \quad \boldsymbol{u}(\boldsymbol{x},0) = \boldsymbol{0}, \tag{26}$$

where $\boldsymbol{x}_{||}$ is the in-plane position vector, $A_{ij} = \varepsilon(i^2 + j^2)^{-\nu/2}\mathscr{N}(i,j)$, $\mathscr{N}$ being a Gaussian distribution, ν the spectral exponent, $\boldsymbol{k}_{ij} = 2\pi/x_{\max}(i\boldsymbol{e}_x + j\boldsymbol{e}_y)$, with $x_{\max}$ the size of the computational domain in the x and y directions, and $\mathscr{U}(i,j)$ the uniform distribution.

Fig. 9 shows snapshots of the time evolution of a three-dimensional Newtonian thin liquid film in the upper row, and the corresponding non-Newtonian film modeled with the Oldroyd-B constitutive equation in the bottom row. In particular, in both simulations the initial height of the film is $h_o/a = 5$, the perturbation amplitude is $\varepsilon = 0.05$, and the precursor height is set to $h_{\text{prec}} = 0.35$. The remaining dimensionless parameters of the Oldroyd-B film are $De = 10$, and $\beta = 0.1$, which might be similar to those reported in ref.[21].

The main quantitative differences between the Newtonian and the viscoelastic film are the characteristic dewetting time, which is given by the linear stability analysis developed in §3 (see Fig. 3), and the height of the drops and rims, which are higher in the Newtonian case. However, the dewetting pattern is qualitatively similar in both scenarios, thus the morphology shown by refs.[21,36,38] cannot be a direct consequence of the viscoelastic behaviour of the film. Indeed, Fig. 6 shows the time evolution of the component σ_{zz} for the viscoelastic film displayed in Fig. 10(*a*-*e*), evidencing that the polymeric stresses remain confined to regions close to the rim, as anticipated by Fig. 5. Therefore, other effects must be taken into account to explain such patterns, namely the residual stresses, the slippage of the film which can be large in glassy films[62?,63], or the viscoplastic nature of the material. Aside from the patterns observed by ref.[21], the advanced post-processing techniques used by ref.[26] could be potentially used here to infer and characterize the viscoelastic properties of the film from the 3D patterns, namely the relaxation time of the polymer chains or the nonlinear material parameters introduced in the Giesekus and FENE-P models. However, this task is out of the scope of the present work.

6 Conclusions and future prospects

Despite the relevance of ultra-thin viscoelastic and glassy coatings, some fundamental questions about their dynamics have remained overlooked. By considering three viscoelastic models, i.e., the Oldroyd-B, Giesekus, and FENE-P models, we have shed light on some aspects of their linear and near-rupture dynamics. In particular, analytical estimations of the rupture times and associated wavelengths of the dewetting patterns are given by means of linear theory in terms of the relevant dimensionless governing parameters. In particular, it is found that such wavelength is independent from the values of the solvent-to-total viscosity ratio and Deborah numbers, therefore being an exclusive function of the Capillary number regardless the rheological model employed. Additionally, by means of two-dimensional numerical simulations of the Stokes equations coupled with non-linear viscoelastic models, we have shown that for times close to the singularity, the Newtonian self-similar regime obtained in our previous work[27] is always achieved. This phenomenon occurs independently of the rheological behaviour of the planar film, the consequence being that the viscoelastic stresses remain confined in a boundary layer placed at the free surface, and whose thickness becomes smaller as breakup is approached. Moreover, we have also performed three-dimensional numerical simulations of a planar viscoelastic film with random initial conditions, to determine if the dewetting patterns are substantially different from their Newtonian counterpart. However, the final morphologies found in both cases film are

qualitatively similar, which means that the viscoelastic rheology is not the cause of the dewetting patterns reported in refs.[21,36,38]. Here we suggest that such morphologies might be a consequence of the residual and thermal stresses, a manifestation of viscoplastic behaviour, or a strong slippage of these rheologically complex films. Although these effects are out of the scope of the present work, their study constitutes an exciting direction for future contributions.

A The analytical expression for the growth rate

The closed-form solution to the dispersion relation (8) for the growth rate is available as follows:

$$\omega = \frac{1}{4\beta\, Ca\, De\, k\left(1+2k^2+\cosh 2k\right)}\left\{8\beta\, Ca\, De k\left(3Ca-k^2\right)\times\right.$$
$$[\sinh(2k)-2k]\left[1+2k^2+\cosh(2k)\right]+$$
$$\left[2k\left(3Ca\, De+2Ca\, k^2+Ca-De\, k^2\right)+\right.$$
$$\left.De\left(k^2-3Ca\right)\sinh 2k+2Ca\, k\cosh 2k\right]^2\Big\}^{1/2}$$
$$-6Ca\, De\, k+3Ca\, De\sinh(2k)-4Ca\, k^3-$$
$$2Ca\, k[1+\cosh(2k)]+2De\, k^3-De\, k^2\sinh(2k). \qquad (27)$$

which is provided here for the first time (to the best of our knowledge). The second root of (8) is always negative for all k. Note that in refs.[28,29] only the dispersion relation (8) is given.

Conflicts of interest

There are no conflicts to declare.

Acknowledgements

This research was funded by the Spanish MCIU-Agencia Estatal de Investigación through project DPI2017-88201-C3-3-R, partly financed through FEDER European funds. Support from the Red Nacional para el Desarrollo de la Microfluídica, RED2018-102829-T, is also acknowledged. A.M.-C. is grateful to Amir Pahlavan for bringing this research line to his attention during his stay in Princeton, and also acknowledges support from the Spanish MECD through the grant FPU16/02562.

Notes and references

1 R. Pattle, *Q. J. Mech. Appl. Math.*, 1959, **12**, 407–409.
2 H. E. Huppert, *J. Fluid Mech.*, 1982, **121**, 43–58.
3 H. E. Huppert, *J. Fluid Mech.*, 1986, **173**, 557–594.
4 O. E. Jensen and J. B. Grotberg, *J. Fluid Mech.*, 1992, **240**, 259–288.
5 D. Halpern and J. B. Grotberg, *J. Fluid Mech.*, 1992, **237**, 1–11.
6 O. E. Jensen and J. B. Grotberg, *Phys. Fluids A: Fluid Dyn.*, 1993, **5**, 58–68.
7 D. Halpern and J. B. Grotberg, *J. Bio. Eng.*, 1993, **115**, 271–277.
8 J. B. Grotberg, *Annu. Rev. Fluid Mech.*, 1994, **26**, 529–571.
9 D. Halpern, O. E. Jensen and J. B. Grotberg, *J. App. Phys.*, 1998, **85**, 333–352.
10 K. J. Cassidy, D. Halpern, B. G. Ressler and J. B. Grotberg, *J.*

35 F. Saulnier, E. Raphaël and P.-G. de Gennes, *Phys. Rev. Lett.*, 2002, **88**, 196101.

36 G. Reiter, M. Hamieh, P. Damman, S. Sclavons, S. Gabriele, T. Vilmin and E. Raphaël, *Nat. Mater.*, 2005, **4**, 754–758.

37 T. Vilmin and E. Raphaël, *EPL*, 2005, **72**, 781–787.

38 S. Gabriele, P. Damman, S. Sclavons, S. Desprez, S. Coppée, G. Reiter, M. Hamieh, S. A. Akhrass, T. Vilmin and E. Raphaël, *J. Polym. Sci. Pol. Phys. Phys.*, 2006, **44**, 3022–3030.

39 A. Vrij, *Discussions of the Faraday Society*, 1966, **42**, 23–33.

40 R. Blossey, *Thin liquid films: dewetting and polymer flow*, Springer Science & Business Media, 2012.

41 H. Hamaker, *Physica*, 1937, **4**, 1058–1072.

42 E. Ruckenstein and R. K. Jain, *J. Chem. Soc., Faraday Trans. 2*, 1974, **70**, 132–147.

43 R. B. Bird, R. C. Armstrong and O. Hassager, *Dynamics of polymeric liquids. Vol. 1: Fluid mechanics*, Wiley, 1987.

44 R. B. Bird, R. C. Armstrong and O. Hassager, *Dynamics of Polymeric Liquids, Vol. 1: Fluid Mechanics, Vol. 2: Kinetic Theory*, Wiley, 1987.

45 R. B. Bird, *Annu. Rev. Fluid Mech.*, 1976, **8**, 13–34.

46 R. B. Bird and J. M. Wiest, *Annu. Rev. Fluid Mech.*, 1995, **27**, 169–193.

47 V. M. Entov and E. J. Hinch, *J. Non-Newtonian Fluid Mech.*, 1997, **72**, 31–53.

48 S. L. Anna and G. H. McKinley, *J. Rheol.*, 2001, **45**, 115–138.

49 G. H. McKinley, *M.I.T. preprint*, 2005.

50 C. Clasen, J. Eggers, M. A. Fontelos, J. Li and G. H. McKinley, *J. Fluid Mech.*, 2006, **556**, 283–308.

51 J. G. Oldroyd, *Proc. R. Soc. Lond. A. Math. Phys. Sci.*, 1958, **245**, 278–297.

52 J. C. Maxwell, *Phil. Trans. R. Soc. Lond.*, 1867, 49–88.

53 H. Jeffreys, *The Earth: London*, 1929.

54 M. A. Fontelos and J. Li, *J. Non-Newtonian Fluid Mech.*, 2004, **118**, 1–16.

55 R. B. Bird, P. J. Dotson and N. L. Johnson, *J. Non-Newtonian Fluid Mech.*, 1980, **7**, 213–235.

56 A. Peterlin, *J. Polym. Sci. Part B: Polym. Lett.*, 1966, **4**, 287–291.

57 H. Giesekus, *J. Non-Newtonian Fluid Mech.*, 1982, **11**, 69–109.

58 P.-G. De Gennes, *Rev. Mod. Phys.*, 1985, **57**, 827.

59 R. K. Jain and E. Ruckenstein, *Journal of Colloid and Interface Science*, 1976, **54**, 108–116.

60 D. Moreno-Boza, A. Martínez-Calvo and A. Sevilla, *arXiv preprint arXiv:2005.04785*, 2020.

61 P. P. Bhat, S. Appathurai, M. T. Harris, M. Pasquali, G. H. McKinley and O. A. Basaran, *Nat. Phys.*, 2010, **6**, 625–631.

62 P.-G. de Gennes, *C. R. Acad. Sci.*, 1979, **228B**, 219.

63 F. Brochard and P. G. De Gennes, *Langmuir*, 1992, **8**, 3033–3037.